Science Advances
AAAS

FRONT MATTER

Title

Hollow Metal Halide Perovskite Nanocrystals with Efficient Blue Emissions

Authors

Michael Worku[1], Yu Tian[1†], Chenkun Zhou[2], Haoran Lin[3], Maya Chaaban[3], Liang-jin Xu[3], Qingquan He[3], Drake Beery[3], Yan Zhou[3], Xinsong Lin[3], Yi-feng Su[4], Yan Xin[4] & Biwu Ma*[1, 2, 3]

Affiliations

[1]Materials Science and Engineering Program, Florida State University, Tallahassee, FL 32306, USA.
[2] Chemical and Biomedical Engineering, FAMU-FSU College of Engineering, Florida State University, Tallahassee, FL 32310, USA.
[3]Department of Chemistry and Biochemistry, Florida State University, Tallahassee, FL 32306, USA.
[4]National High Magnetic Field Laboratory, Florida State University, Tallahassee, FL 32310, USA.
[†]Current Address: Global Solar Energy, Tucson, AZ, 85747, USA.
Corresponding author email: bma@fsu.edu

Summary

A novel hollow nanostructure enables color tuning of metal halide perovskites with blue emissions from cesium lead bromide.

Abstract

Metal halide perovskite nanocrystals (NCs) have emerged as new generation light emitting materials with narrow emissions and high photoluminescence quantum efficiencies (PLQEs). Various types of perovskite NCs, e.g. platelets, wires, and cubes, have been discovered to exhibit tunable emission across the whole visible spectrum. Despite remarkable advances in the field of metal halide perovskite NCs over the last few years, many nanostructures in inorganic NCs have not yet been realized in metal halide perovskites, and producing highly efficient blue emitting perovskite NCs remains challenging and of great interest. Here we report, for the first time, the discovery of highly efficient blue emitting cesium lead bromide perovskite ($CsPbBr_3$) NCs with hollow structures. By facile solution processing of cesium lead bromide perovskite precursor solution containing additional ethylenediammonium bromide and sodium bromide, in-situ formation of hollow $CsPbBr_3$ NCs with controlled particle and pore sizes is realized. Synthetic

control of hollow nanostructures with quantum confinement effect results in color tuning of $CsPbBr_3$ NCs from green to blue with high PLQEs of up to 81 %.

MAIN TEXT

Introduction

Metal halide perovskite nanocrystals (NCs) have received great attention as an emerging class of light emitting materials for their narrow emission, exceptional photoluminescence quantum efficiencies (PLQEs) and color tunablitity.(*1-4*) Various approaches have recently been developed to achieve synthetic control of the composition, size, and shape of perovskite NCs to obtain emission colors covering the whole visible spectrum, from deep blue to near-infrared.(*5-14*) For instance, by manipulating the quantum size effect, the emission of $CsPbBr_3$ NCs can be tuned from green for NCs with sizes larger than the exciton bohr radius (~7 nm), to deep blue for quantum dots, nanowires, and nanoplatelets with strong quantum confinement.(*15-20*) Several recent studies have demonstrated nanocrystal size control within the quantum confinement regime by introducing organic salts,(*21*) controlling the acid-base environment,(*22*) varying Pb to halide ration,(*23*) etc.(*24*) Although highly efficient perovskite NCs can be synthesized using colloidal methods, preserving the high PLQEs during transfer of colloidal NCs to thin films for device integration has been challenging.(*3*) On the other hand, in-situ formation of highly efficient perovskite NCs is not trivial either, because of the limited control on particle size, monodispersity, and surface passivation. This is even more relevant in blue emitting perovskite NCs, which are generally in the size range of 4-6 nm for $CsPbBr_3$ and thus possess high surface area to volume ratios that readily lead to high surface defect density and low PLQEs.

Hollow NCs, nanostructures with pores, provide an additional degree of freedom to exploit the quantum size effect by controlling pore and grain sizes. Several classes of hollow NCs have previously been reported, e.g. metal chalcogenides,(*25, 26*) metal oxides,(*27, 28*) metal nanoparticles(*29*), with applications in catalysis and energy storage. To the best of our knowledge, hollow metal halide perovskite NCs have not yet been discovered. Here, we report a novel approach to achieving highly efficient blue emission from $CsPbBr_3$ perovskite NCs by creating hollow nanostructures with controlled sizes. By spin-casting a mixture solution containing cesium bromide (CsBr), lead bromide ($PbBr_2$), ethylenediammonium bromide ($(H_3N(CH_2)_2NH_3)Br_2$), and sodium bromide (NaBr), in-situ formation of hollow $CsPbBr_3$ perovskite NCs was achieved. It was found that $[NH_3(CH_2)_2NH_3]^{2+}$ (EDA^{2+}) cations act as both surface passivation ligands and A-site cations that lead to the formation of randomly oriented Pb^{2+} vacancies. And the presence of Na^+ along with EDA^{2+} cations produces hollow nanostructures. By carefully controlling the $EDABr_2$ and NaBr content, size tuning of pore and grain radii of hollow $CsPbBr_3$ perovskite NCs was achieved, resulting in emission color tuning from green (525 nm) to blue (459 nm) with high PLQEs of up to 81 %. Our work introduces a new nanostructure to the family of metal halide perovskites, showing once again their exceptional structural versatility. The hollow perovskite NCs with tunable optical and electronic properties may have potential applications in various optoelectronic applications, for instance, blue light-emitting diodes (LEDs).

Results

The schematic diagram of a one-step spin-casting process for the preparation of metal halide perovskite thin films is shown in Fig. 1A. Briefly, metal halide perovskite precursors (CsBr and $PbBr_2$) mixed with $EDABr_2$ and NaBr at controlled ratios, were spun cast on glass substrates, followed by low temperature thermal annealing at around 100 ºC (see Experimental Details in Methods). By fixing the concentration of NaBr to 3 mol % with respect to the perovskite precursors and varying the molar ratio of $EDABr_2$ (from 0 to 1.2 with respect to the perovskite precursors), uniform and smooth thin films were produced as evidenced by the atomic force microscopy (AFM) images (Fig. S1A-F). The thickness of these thin films was measured to be 42 $\pm$ 8 nm (Fig. S2). The thin films were transparent under ambient light but displayed green and blue emissions under UV irradiation (Fig, 1B). The photophysical properties of the thin films were investigated via UV-Vis absorption, steady-state photoluminescence (PL) and time-resolved photoluminescence (TRPL) spectroscopy, as well as photoluminescence quantum efficiency (PLQE) measurements. The absorption onset and the photoluminescence emission peaks were steadily shifted to lower wavelengths with the increase of the $EDABr_2$ concentration, while keeping the NaBr content constant (Fig. 1C). This blue shift of emission spectra was also associated with a pronounced increase in the PL decay lifetimes (Fig. 1D and Table S1), indicating the role of EDA^{2+} cations in surface defect passivation.(*30*) The defect passivation is further supported by PLQE measurements, where samples containing increasing amounts of $EDABr_2$ showed a steep increase (Fig. 1E), with a peak PLQE of 72 % at 478 nm for the sample with 1:1 ratio of $EDABr_2$ to the perovskite precursors.

To better understand the effects of NaBr and $EDABr_2$ on the photophysical properties of perovskite thin films, we systemically adjusted the concentration of NaBr with and without the presence of $EDABr_2$, and vice versa. Changing the NaBr content within the precursor solution, (while keeping the concentration of $EDABr_2$ constant at 1:1 ratio with respect to the perovskite precursors) also afforded emission color tuning, from 498 nm for the sample without NaBr to 459 nm for that containing 4 mol% of NaBr (Fig. S3A). However, the PLQEs steadily declined with the increase of NaBr concentration (Table S2). Controlling the content of NaBr without the presence of $EDABr_2$, however, had little-to-no effect on the photoluminescence spectrum and PLQE (Fig. S4A). These results suggested that NaBr did not play a passivation role in the thin films. Moreover, by controlling the $EDABr_2$ content without the presence of NaBr, limited color tuning was achieved, with the blue shift saturating at around 498 nm (Fig. S4B). To reveal the structure-property relationships and understand the roles of Na^+ and EDA^{2+} cations in these systems, we investigated four representative samples in detail, whose compositions and photophysical properties are summarized in Table 1. The sample $CsPbBr_3$ was prepared from the solution containing perovskite precursors without the addition of NaBr and $EDABr_2$, the sample $CsPbBr_3$–Na was prepared from the solution containing perovskite precursors and 3 mol % NaBr, the sample EDA5 was prepared from the solution containing perovskite precursors and $EDABr_2$ at 1:1 ratio; the sample EDA5–Na was prepared from the solution containing perovskite precursors and $EDABr_2$ at 1:1 ratio as well as 3 mol% NaBr.

The structural properties of the four samples were investigated by selected area electron diffraction (SAED) and x-ray powder diffraction (XRD) (Fig. 2A-B). The sample $CsPbBr_3$ was identified to have an orthorhombic phase (space group Pnma) and the diffraction peaks were indexed accordingly. Apart from small peak shifts (Fig. 2C-D), the other three samples displayed the same diffraction patterns without any sign of low-dimensional or non-perovskite phases, indicating the formation of a 3D perovskite structure. The shifts of the diffraction peaks can be ascribed to unit cell contraction or expansion. For the sample $CsPbBr_3$-Na, slight shifts to higher

diffraction angles were observed ($\Delta 2\theta \approx 0.022°$ for the (121) and $\approx 0.054°$ for the (202) planes), which was not surprising as the incorporation of small Na^+ cations (ionic radius of 116 pm) at the A-site could lead to unit cell contraction.(*31*) This lattice contraction was further confirmed by X-ray photoelectron spectroscopy (XPS), which showed a shift of the Pb 4f and Br 3d photoelectron spectra to higher binding energies in comparison to the control sample (Fig. 2E-F). This indicates an increased Pb-Br interaction as a result of reduced bond length. In contrast, the diffraction peaks for the samples EDA5 and EDA5-Na displayed small shifts to lower 2θ as a result of unit cell expansion. This shift of diffraction peaks could be well explained to result from the incorporation of large EDA^{2+} cations (ionic radius 333 pm (*32*)) within the 3D perovskite structure, which has previously been shown in other halide perovskites.(*32-36*) Prior reports had proposed lattice strain caused by Pb-X (X = Cl, Br, I) bond elongation (*35*) and the formation of a hollow 3D structure (*32*) as mechanisms to explain lattice expansion upon the incorporation of large organic cations. Moreover, because the valence band maximum of ABX_3 type 3D halide perovskites is an antibonding hybrid state of the metal s and halide p orbitals, reduced interaction of the B^{2+} and X^- ions, due to either bond elongation or discontinuities, would lead to energy band gap increase.(*37*)

XPS was employed to probe changes of the Pb-Br interactions in the samples EDA5 and EDA5-Na. Lattice expansion caused by Pb-Br bond elongation would shift the Pb 4f and Br 3d photoelectron spectra to lower binding energies (*38, 39*) without affecting Br/Pb ratio. In contrast, a hollow structure with Pb^{2+} vacancies should display higher Br/Pb ratio but little-to-no change in binding energies of the core levels. Pb 4f and Br 3d photoelectron spectra for EDA5 show no shift compared to those from $CsPbBr_3$ (Fig. 2E-F). Moreover, quantitative analysis of the XPS spectra showed Br/Pb ratio increased significantly with the incorporation of EDA^{2+} (~ 3.97 for the sample EDA5) compared to the sample $CsPbBr_3$ (~2.27), suggesting the formation of Pb^{2+} vacancies and a hollow 3D structure. We attribute the below-nominal Br/Pb ratio in pure $CsPbBr_3$ to the presence of high surface defect density as corroborated by the short average PL decay lifetime. Energy dispersive x-ray fluorescence (EDXRF) was also conducted to probe the relative concentrations of Pb^{2+} and Br^- in the studied samples. Br $K_{\alpha 1}$ and Br $K_{\beta 1}$ as well as Pb $L_{\alpha 1}$ and Pb $L_{\beta 1}$ lines from the four samples are shown in Fig. S5A. To quantify the molar ratios between the different components, the intensity vs concentration scatter plots for the standards (fit using a linear equation) were used as calibration curves (Fig. S5B-D). The Br/Pb ratio in EDA5 obtained through EDXRF displayed a similar trend as what was observed from the XPS quantitative analysis. This confirms the formation of Pb^{2+} vacancies. The blue-shift of emissions for the $CsPbBr_3$ thin films upon the addition of $EDABr_2$ is also consistent with what was observed in hollow 3D $MASnI_3$, $MAPbI_3$ and $FASnI_3$ perovskites.(*32-34, 40*)

Increasing the EDA^{2+} content also led to decreasing grain sizes as evidenced by the XRD peak broadening (Fig. S6). The nanocrystal formation and surface defect passivation by EDA^{2+} cations resulted in significantly increased PLQEs, with the highest value recorded for EDA5 at ~ 81%. Overall, EDA^{2+} cations can form small crystalline domains of $CsPbBr_3$, passivate their surfaces, and penetrate the lattice to form hollow 3D structures. Further lattice expansion was observed for the sample EDA5-Na, which showed significantly blue shifted emission as compared to the other samples. We speculate Na^+ cations occupy interstitial sites within the perovskite structure as has been reported for alkali ions in organo-metal halide perovskites,(*41*) because Na^+ cations are too small to create more Pb^{2+} vacancies as seen with EDA^{2+}. A slight shift to higher binding energies was also observed for Br 3d and Pb 4f core orbitals of EDA5-Na. Because of the increased lattice parameter for EDA5-Na, improved orbital overlap between Pb^{2+} and Br^- ions cannot explain the observed peak shift in the photoelectron spectra. However, the

presence of interstitial defects has previously been shown to result in increased lattice parameters and photoelectron spectra shift to higher binding energies.(*42*) Thus, we ascribe the observed lattice expansion and photoelectron spectra shift to the presence of Na^+ interstitials. Hence, EDA5-Na samples could be composed of hollow 3D structures with additional Na^+ interstitials.

In order to directly visualize the effects of the different ions on the microstructural properties of these samples, we used transmission electron microscopy (TEM) and high resolution TEM (HRTEM) to characterize the thin films. TEM images of $CsPbBr_3$-Na, EDA5 and EDA5-Na clearly indicate the formation of perovskite NCs (Fig. 4A). Particle size distribution analysis revealed median sizes of around 40 nm, 12 nm, and 17 nm for $CsPbBr_3$-Na, EDA5 and EDA5-Na, respectively. As the median particle size of EDA5-Na is still much larger than the exciton bohr radius of $CsPbBr_3$ (~ 7 nm), blue emission from small quantum confined $CsPbBr_3$ NCs could not be the case here. With HRTEM, large pores at the center of $CsPbBr_3$ NCs with a median size of 4.25 nm were observed in EDA5-Na. The NCs with pores, or hollow NCs, could be clearly observed throughout the whole film (Fig S7A-D). These hollow NCs were not present in $CsPbBr_3$-Na or EDA5 (Fig. 3B and Fig. S8). The median shell thickness of these hollow $CsPbBr_3$ NCs was found to be 6.5 nm (inset of Fig. S7C). This shell thickness is slightly larger than the grain size needed for $CsPbBr_3$ to possess an emission energy of ~ 2.6 eV (~ 477 nm), i.e. ~ 6 nm.(*5*) However, aside from the quantum confinement effect, the hollow 3D crystal structure of EDA5-Na will also contribute to the energy band gap widening, as discussed above. Thus, we ascribe the observed optical band gap widening and emission peak shift to the combined effect of quantum confinement and a hollow 3D crystal structure. These hollow nanostructures answer how the optical band gap of $CsPbBr_3$ NCs could be tuned while the size of the NC grains was still well above the exciton bohr radius of ~ 7 nm.

The TEM and HRTEM images were further analyzed to confirm that the "lighter" regions were not results of inter-grain voids, sample preparation artifacts or electron beam damage. Fast Fourier transform of TEM and STEM images of mono-grain hollow nanocrystals show single sets of spots indicating the single crystalline nature of these nanocrystals (Fig. S9). Moreover, the absence of spots from multiple grains conclusively proves that the pores are not a result of inter-grain voids. To exclude the TEM sample preparation as the source of the observed unique nanostructures, we conducted the TEM characterization using an alternative sample preparation technique (Fig. S10). The collected TEM images were consistent with what was observed using the "scratch and sonicate" TEM sample preparation technique (experimental details in Methods), confirming that these nanostructures were not sample preparation artifacts. Moreover, the low contrast regions in these grains do not resemble the products reported to arise from electron beam damage (Pb rich nanoparticles).(*43*) In addition, TEM images taken 10 s apart for a total of 60 s show that there is little change in the microstructure of the sample, indicating that the pores are not results of electron beam damage (Fig. S11).

Previous studies on hollow NCs have attributed their formation to nanoscale Kirkendall effect(*25, 44*), Ostwald ripening(*28*), galvanic replacement(*27*) and cation exchange(*26*). To gain a better understanding on the roles played by the different components during the growth of these hollow nanocrystals, we used a combination of surface and bulk sensitive techniques (XPS and energy-dispersive X-ray spectroscopy (EDX)). It was found that electrons from Cs $3d_{5/2}$, C 1s of C-N bond and N 1s orbitals were detectable in XPS (Fig. S12), indicating the presence of Cs^+ and EDA^{2+} ions on or near the surface. While electrons from Na 1s orbital were readily discernable in XPS for $CsPbBr_3$-Na, they were not observed in EDA5-Na (Fig. S12). In contrast, EDX spectrum of EDA5-Na confirmed the presence of Na^+ ions within the bulk (Fig. S13). These results suggest

that Na^+ cations were located deep in the shell or within the core of the hollow NCs. Based on the changes observed in the lattice, surface chemistry and microstructure of the hollow NCs as compared to the regular NCs, we propose a formation mechanism (Fig. 4A), in which the diffusion of Na^+ ions from the surface to the core selectively draws Br^- anions from the perovskite lattice to the surface, (*45*) reducing the coordination number of Pb^{2+} cations. Because undercoordinated ions generally display higher free energy compared to those that are fully coordinated, Pb^{2+} ions will likely diffuse to lattice sites with higher coordination number driven by the free energy landscape. Although the diffusion of Pb^{2+} ions has been reported to possess a high diffusion barrier of ~ 2.3 eV, the presence of Pb^{2+} vacancies due to the incorporation EDA^{2+} could lower this energy barrier.(*46*) The diffusion of Pb^{2+} cations will be associated with vacancy migration in the opposite direction resulting in vacancy coalescence and void formation. To test the proposed mechanism, we introduced NaBr before thin film deposition in the form of a 20 nm thin film on glass substrate. The EDA5 precursor was then deposited on top of the NaBr layer. The obtained thin film displayed a broad PL spectrum that can be deconvoluted to the spectra of EDA5 and EDA5 containing 2 mol % NaBr (Fig. S14C). This result indicates that, Na^+ ions can diffuse into the EDA5 thin film to form hollow nanocrystals. Overall, the effects of individual additives (NaBr and $EDABr_2$) and their combination on the morphological and optical properties of $CsPbBr_3$ can be summarized in Fig. 4B: the addition of only Na^+ has little-to-no effect on the crystalline lattice, the addition of only EDA^{2+} creates hollow 3D structures and the addition of both Na^+ and EDA^{2+} leads to the formation of hollow perovskite NCs.

With the understanding of the roles of the different ions, we demonstrated rational control of the particle and pore sizes of $CsPbBr_3$ hollow NCs, and subsequently their optical properties, by controlling the Na^+ and EDA^{2+} contents. The increase in Na^+ content (in the presence of EDA^{2+} 1:1 with the perovskite precursors) had no significant effect on grain size, but generally led to larger pore sizes from a median pore size of 3.2 nm for samples with 1 mol % NaBr to 4.8 nm for those containing 4 mol % of NaBr (Fig. S15). This pore size increase in turn resulted in a narrower shell thickness and a corresponding optical band gap widening. Conversely, increasing the EDA^{2+} concentration (in the presence of Na^+) had no obvious influence on the pore size, but led to the reduction of the particle sizes. The median particle size decreased from 19 nm to 17 nm for the samples prepared with of 0.4 and 1.2 molar ratios of $EDABr_2$, while keeping the NaBr content constant at 3 mol % (Fig. S16).

Discussion

Obtaining a mono-grain thick thin film could lead to further insight into the role of each component by, for instance, allowing an accurate elemental mapping which can conclusively show the distribution of each component. However, in-situ formation of mono-grain thick nanocrystalline thin film was found to be a nontrivial task. Thus, we believe future effort in this area should be directed toward colloidal synthesis of these multi-component hollow nanocrystals. Free-standing nanocrystals would not only lend a major insight into the morphology of these hollow structures but will also provide a path to investigate their formation through in-situ microscopy methods.(*47*) Moreover, the increased degrees of freedom in colloidal synthesis of nanocrystals may also lead to the discovery of other exotic structures.

In summary, by carefully choosing appropriate organic and alkali metal salts, light emitting thin films containing hollow perovskite nanocrystals can be prepared via facile solution processing. The organic cations not only penetrate the perovskite lattice to create vacancies, but also passivate the surfaces of the perovskite nanocrystals. The small alkali metal cations can diffuse throughout the perovskite lattice to assist the formation of hollow structures with the

presence of large organic cations. As a result, quantum confinement can be realized in hollow perovskite nanocrystals with controlled pore sizes and shell thicknesses, which exhibit highly tunable emission with high PLQEs. Our work represents a groundbreaking advance in the field of metal halide perovskite nanocrystals, from well-developed nanostructures with positive curvatures to novel hollow structures, which will stimulate exploration of other nanostructures with remarkable and unique properties. Applications of hollow perovskite nanocrystals in various types of optoelectronic devices are envisioned in the near future.

Materials and Methods

Materials. Lead (II) bromide (99.999 %), cesium bromide (99%), ethylenediamine (99 %), hydrobromic acid (48 wt. % in H_2O), sodium bromide (99 %) and dimethyl sulfoxide (99.9%) were purchased from Sigma-Aldrich. All reagents and solvents were used without further purification unless otherwise stated.

Synthesis of $C_2N_2H_{10}Br_2$ ($EDABr_2$). Ethylenediamine (1 equiv.) and 48 wt. % hydrobromic acid (2.1 equiv.) were combined in ethanol at 0 °c. After 30 minutes, white precipitate was extracted through evaporation of the solvent using a rotary evaporator. The white precipitate was washed with diethyl ether twice and was left to dry in a desiccator overnight before use. The salt was stored in a glovebox.

Thin film processing. 0.2 mmol CsBr and 0.2 mmol $PbBr_2$ were dissolved in 1 ml of DMSO to make the perovskite precursor solution. $EDABr_2$ was added to the perovskite precursor solution in varying concentrations from 0 to 1.2 molar ratio. The Na^+ content in the perovskite precursor solution was controlled by varying the amount of NaBr from 0 to 4 mol%. ITO substrates were purchased from Thin Film Devices (any glass substrate that does not contain sodium would work). Before use, they were sequentially cleaned by sonicating in detergent (Hellmanex III) water, deionized water, acetone and isopropanol for 15 minutes and were dried in an oven overnight. The substrates (bare-side) were then cleaned under UV-Ozone treatment and transported into a glovebox for one-step spin coating of the precursor solution at 3000 RPM for 60 s. Subsequently, the films were annealed at 100 °C for 20 minutes.

Atomic Force Microscopy. AFM images were taken on a Bruker Icon scanning probe microscope in tapping mode.

Photoluminescence spectroscopy. Steady-state PL was carried out using an Edinburgh FS5 steady state spectrometer with a 150 W xenon lamp at an excitation wavelength of 365 nm. TRPL was collected using Time Correlated Single Photon Counting (TCSPC) for 10,000 counts. Excitation was provided by an Edinburgh EPL-360 picosecond pulsed diode laser. The PL decay was fit using a biexponential decay curve for $CsPbBr_3$ $CsPbBr_3$-Na and EDA5 and triexponential decay function for EDA5-Na. The average lifetime was obtained from the bi- or tri-exponential decays according to equation 1.

$$\tau_{ave} = \Sigma\alpha_i\tau_i^2/\Sigma\alpha_i\tau_i,\ i = 1, 2, 3 \quad (1)$$

where τ_i represents the decay time and α_i represents the amplitude of each component.

Absorption spectrum measurements. Absorption spectra were obtained using an Agilent Technologies Cary 5000 UV-Vis-NIR spectrophotometer.

Photoluminescence quantum efficiency (PLQE). PLQE measurements were performed in accordance to what has been reported previously.(*48*) Briefly, a Hamamatsu Quantaurus-QY Spectrometer (Model C11347-11) equipped with a xenon lamp, an integrating sphere sample chamber and a CCD detector. The PLQEs were calculated by the equation: $\eta QE = \frac{I_S}{E_R - E_S}$, in which

I_S represents the luminescence emission spectrum of the sample, E_R is the spectrum of the excitation light for the reference (empty substrate) , and E_S is the excitation spectrum for exciting the sample. The PLQE measurements were done consecutively and a density of 0.3 mW/cm^2 at an excitation wavelength of 365 nm was used for all samples.

Powder X-ray diffraction (XRD). XRD patterns were obtained using a Siemens D500 powder diffractometer equipped with a Cu Kα x-ray source. Diffraction patterns were recorded from 5° to 40° 2θ with a step size of 0.05° under a tube current of 30 mA and tube voltage of 40 KV.

Transmission Electron Microscopy images (TEM). Microstructural characterization was performed using transmission electron microscopy (TEM), on a JEOL JEM-ARM200cF at 200kV. TEM samples were prepared by scraping thin films from substrate and dispersing the powder in a non-polar solvent (Hexane). The dispersion was sonicated for 10 minutes to ensure uniform distribution before dropping it on a 200 mesh Cu grid. Alternatively, Cu grids were pressed face-down on thin films prepared on PDMS substrates, followed by applying a single drop of 2-propanol on the Cu grid. The Cu grids were then picked up using fine tweezes before the solvent completely evaporated. TEM image analysis was performed in Gatan microscopy software suite.

X-ray photoelectron spectroscopy (XPS). XPS was conducted using a PHI 5000 series XPS equipped with a dual anode x-ray source. For our purpose, Al Kα radiation with a photon energy of 1486.6 eV at a take-off angle of 45° and a pass energy of 35.75 eV were used. Charge compensation was performed using adventitious C 1s peak (284.6 eV). Spectra background were fit and subtracted using a integrated Shirley function. XPS curves were deconvoluted using a Voight peak function for metal core electron spectra and gaussian peak functions for the rest.

Energy Dispersive X-ray Fluorescence. EDXRF was performed using a Panalytical Epsilon 3 spectrometer equipped with a rhodium X-ray tube and a silicon drift detector.

Supplementary Materials

Fig. S1. Atomic Force Microscopy images thin films.

Fig. S2. Thin film thickness.

Fig. S3. The effect of NaBr on photophysical properties of CsPbBr3 containing EDABr2.

Fig. S4. Photoluminescence spectra of CsPbBr3 thin films with addition of NaBr or $EDABr_2$.

Fig. S5. Energy Dispersive X-ray fluorescence.

Fig. S6. XRD characterization of thin films with varying EDABr2 content

Fig. S7. Microstructural characterization of EDA5-Na.

Fig. S8. TEM images of thin films.

Fig. S9. Mono-grain hollow nanocrystals.

Fig. S10. Alternative TEM sample preparation.

Fig. S11. TEM image as a function of electron beam irradiation time.

Fig. S12. XPS characterization of thin films.

Fig. S13. Energy-dispersive x-ray spectra of EDA5-Na.

Fig S14. Alternative processing of hollow nanocrystal thin films.

Fig S15. The effect of NaBr content on microstructure.

Fig S16. The effect of EDABr2 content on microstructure.

Table S1 Composition and photophysical properties of samples with varying EDABr2 content.

Table S2. Composition and photophysical properties of samples with varying NaBr content.

Table S3. Atomic concentrations of samples through XPS.

Table S4. Quantitative analysis results of EDXRF.

References and Notes

1. M. V. Kovalenko, L. Protesescu, M. I. Bodnarchuk, Properties and potential optoelectronic applications of lead halide perovskite nanocrystals. *Science* **358**, 745-750 (2017).
2. X. H. He, Y. C. Qiu, S. H. Yang, Fully-Inorganic Trihalide Perovskite Nanocrystals: A New Research Frontier of Optoelectronic Materials. *Adv. Mater.* **29**, (2017).
3. J. Shamsi, A. S. Urban, M. Imran, L. De Trizio, L. Manna, Metal Halide Perovskite Nanocrystals: Synthesis, Post-Synthesis Modifications, and Their Optical Properties. *Chem. Rev.* **119**, 3296-3348 (2019).
4. J. M. Huang, M. L. Lai, J. Lin, P. D. Yang, Rich Chemistry in Inorganic Halide Perovskite Nanostructures. *Adv. Mater.* **30**, (2018).
5. L. Protesescu *et al.*, Nanocrystals of Cesium Lead Halide Perovskites (CsPbX3, X = Cl, Br, and I): Novel Optoelectronic Materials Showing Bright Emission with Wide Color Gamut. *Nano Lett.* **15**, 3692-3696 (2015).
6. I. Levchuk *et al.*, Brightly Luminescent and Color-Tunable Formamidinium Lead Halide Perovskite FAPbX(3) (X = Cl, Br, I) Colloidal Nanocrystals. *Nano Lett.* **17**, 2765-2770 (2017).
7. D. Amgar, A. Stern, D. Rotem, D. Porath, L. Etgar, Tunable Length and Optical Properties of CsPbX3 (X = Cl, Br, I) Nanowires with a Few Unit Cells. *Nano Lett.* **17**, 1007-1013 (2017).
8. A. Z. Pan *et al.*, Insight into the Ligand-Mediated Synthesis of Colloidal CsPbBr3 Perovskite Nanocrystals: The Role of Organic Acid, Base, and Cesium Precursors. *Acs Nano* **10**, 7943-7954 (2016).
9. D. D. Zhang *et al.*, Ultrathin Colloidal Cesium Lead Halide Perovskite Nanowires. *J. Am. Chem. Soc.* **138**, 13155-13158 (2016).
10. D. D. Zhang *et al.*, Synthesis of Composition Tunable and Highly Luminescent Cesium Lead Halide Nanowires through Anion-Exchange Reactions. *J. Am. Chem. Soc.* **138**, 7236-7239 (2016).
11. D. D. Zhang, S. W. Eaton, Y. Yu, L. T. Dou, P. D. Yang, Solution-Phase Synthesis of Cesium Lead Halide Perovskite Nanowires. *J. Am. Chem. Soc.* **137**, 9230-9233 (2015).
12. Y. Bekenstein, B. A. Koscher, S. W. Eaton, P. D. Yang, A. P. Alivisatos, Highly Luminescent Colloidal Nanoplates of Perovskite Cesium Lead Halide and Their Oriented Assemblies. *J. Am. Chem. Soc.* **137**, 16008-16011 (2015).

13. Q. A. Akkerman *et al.*, Tuning the Optical Properties of Cesium Lead Halide Perovskite Nanocrystals by Anion Exchange Reactions. *J. Am. Chem. Soc.* **137**, 10276-10281 (2015).
14. Z. Yuan, Y. Shu, Y. Xin, B. W. Ma, Highly luminescent nanoscale quasi-2D layered lead bromide perovskites with tunable emissions. *Chem. Commun.* **52**, 3887-3890 (2016).
15. Z. Li, L. Kong, S. Huang, L. Li, Highly Luminescent and Ultrastable CsPbBr3 Perovskite Quantum Dots Incorporated into a Silica/Alumina Monolith. *Angew. Chem. Int. Ed. Engl.* **56**, 8134-8138 (2017).
16. V. Malgras, J. Henzie, T. Takei, Y. Yamauchi, Stable Blue Luminescent CsPbBr3 Perovskite Nanocrystals Confined in Mesoporous Thin Films. *Angew Chem Int Edit* **57**, 8881-8885 (2018).
17. B. J. Bohn *et al.*, Boosting Tunable Blue Luminescence of Halide Perovskite Nanoplatelets through Postsynthetic Surface Trap Repair. *Nano Lett.* **18**, 5231-5238 (2018).
18. Y. B. Xu *et al.*, Synthesis of ultrasmall CsPbBr3 nanoclusters and their transformation to highly deep-blue-emitting nanoribbons at room temperature. *Nanoscale* **9**, 17248-17253 (2017).
19. H. W. Huang *et al.*, Atomically thin cesium lead bromide perovskite quantum wires with high luminescence. *Nanoscale* **9**, 104-108 (2017).
20. Y. Wu *et al.*, In Situ Passivation of PbBr64- Octahedra toward Blue Luminescent CsPbBr3 Nanoplatelets with Near 100% Absolute Quantum Yield. *Acs Energy Lett* **3**, 2030-2037 (2018).
21. A. Dutta, S. K. Dutta, S. Das Adhikari, N. Pradhan, Tuning the Size of CsPbBr3 Nanocrystals: All at One Constant Temperature. *Acs Energy Lett* **3**, 329-334 (2018).
22. G. Almeida *et al.*, Role of acid–base equilibria in the size, shape, and phase control of cesium lead bromide nanocrystals. *Acs Nano* **12**, 1704-1711 (2018).
23. Y. Dong *et al.*, Precise control of quantum confinement in cesium lead halide perovskite quantum dots via thermodynamic equilibrium. *Nano Lett.* **18**, 3716-3722 (2018).
24. Y.-H. Kim *et al.*, Highly efficient light-emitting diodes of colloidal metal–halide perovskite nanocrystals beyond quantum size. *Acs Nano* **11**, 6586-6593 (2017).
25. Y. D. Yin *et al.*, Formation of hollow nanocrystals through the nanoscale Kirkendall Effect. *Science* **304**, 711-714 (2004).
26. D. H. Son, S. M. Hughes, Y. Yin, A. P. Alivisatos, Cation exchange reactions in ionic nanocrystals. *Science* **306**, 1009-1012 (2004).
27. M. H. Oh *et al.*, Galvanic Replacement Reactions in Metal Oxide Nanocrystals. *Science* **340**, 964-968 (2013).
28. X. W. Lou, Y. Wang, C. L. Yuan, J. Y. Lee, L. A. Archer, Template-free synthesis of SnO2 hollow nanostructures with high lithium storage capacity. *Adv. Mater.* **18**, 2325-+ (2006).
29. Y. Yin, C. Erdonmez, S. Aloni, A. P. Alivisatos, Faceting of nanocrystals during chemical transformation: From solid silver spheres to hollow gold octahedra. *J. Am. Chem. Soc.* **128**, 12671-12673 (2006).
30. S. J. Lee *et al.*, Amine-Based Passivating Materials for Enhanced Optical Properties and Performance of Organic Inorganic Perovskites in Light-Emitting Diodes. *J Phys Chem Lett* **8**, 1784-1792 (2017).
31. M. Abdi-Jalebi *et al.*, Dedoping of Lead Halide Perovskites Incorporating Monovalent Cations. *Acs Nano* **12**, 7301-7311 (2018).

32. I. Spanopoulos *et al.*, Unraveling the Chemical Nature of the 3D "Hollow" Hybrid Halide Perovskites. *J. Am. Chem. Soc.* **140**, 5728-5742 (2018).
33. W. J. Ke *et al.*, Efficient Lead-Free Solar Cells Based on Hollow {en}MASnI(3) Perovskites. *J. Am. Chem. Soc.* **139**, 14800-14806 (2017).
34. W. J. Ke *et al.*, Enhanced photovoltaic performance and stability with a new type of hollow 3D perovskite {en}FASnI(3). *Sci Adv* **3**, (2017).
35. J. F. Lu *et al.*, Diammonium and Monoammonium Mixed-Organic-Cation Perovskites for High Performance Solar Cells with Improved Stability. *Adv Energy Mater* **7**, (2017).
36. M. Daub, H. Hillebrecht, Tailoring the Band Gap in 3D Hybrid Perovskites by Substitution of the Organic Cations: (CH3NH3)(1-2y)(NH3(CH2)(2)NH3)(2y)Pb1-yI3 (0 <= y <= 0.25). *Chem-Eur J* **24**, 9075-9082 (2018).
37. R. Prasanna *et al.*, Band Gap Tuning via Lattice Contraction and Octahedral Tilting in Perovskite Materials for Photovoltaics. *J. Am. Chem. Soc.* **139**, 11117-11124 (2017).
38. J. K. Nam *et al.*, Potassium Incorporation for Enhanced Performance and Stability of Fully Inorganic Cesium Lead Halide Perovskite Solar Cells. *Nano Lett.* **17**, 2028-2033 (2017).
39. M. Liu *et al.*, Aluminum-Doped Cesium Lead Bromide Perovskite Nanocrystals with Stable Blue Photoluminescence Used for Display Backlight. *Adv Sci* **4**, (2017).
40. Z. Chen *et al.*, Methylammonium, formamidinium and ethylenediamine mixed triple-cation perovskite solar cells with high efficiency and remarkable stability. *J Mater Chem A* **6**, 17625-17632 (2018).
41. J. Cao, S. X. Tao, P. A. Bobbert, C. P. Wong, N. Zhao, Interstitial Occupancy by Extrinsic Alkali Cations in Perovskites and Its Impact on Ion Migration. *Adv. Mater.* **30**, (2018).
42. T. Nishimatsu *et al.*, Prediction of XPS spectra of silicon self-interstitials with the all-electron mixed-basis method. *Physica B: Condensed Matter* **340**, 570-574 (2003).
43. Z. Y. Dang *et al.*, In Situ Transmission Electron Microscopy Study of Electron Beam-Induced Transformations in Colloidal Cesium Lead Halide Perovskite Nanocrystals. *Acs Nano* **11**, 2124-2132 (2017).
44. W. S. Wang, M. Dahl, Y. D. Yin, Hollow Nanocrystals through the Nanoscale Kirkendall Effect. *Chem. Mater.* **25**, 1179-1189 (2013).
45. M. Abdi-Jalebi *et al.*, Maximizing and stabilizing luminescence from halide perovskites with potassium passivation. *Nature* **555**, 497-501 (2018).
46. A. Walsh, S. D. Stranks, Taking control of ion transport in halide perovskite solar cells. *Acs Energy Lett* **3**, 1983-1990 (2018).
47. Y. Zhou, O. S. Game, S. Pang, N. P. Padture, Microstructures of Organometal Trihalide Perovskites for Solar Cells: Their Evolution from Solutions and Characterization. *J Phys Chem Lett* **6**, 4827-4839 (2015).
48. J. C. deMello, H. F. Wittmann, R. H. Friend, An improved experimental determination of external photoluminescence quantum efficiency. *Adv. Mater.* **9**, 230-& (1997).

Acknowledgments: General: The authors thank Dr. Eric Lochner for help with XPS measurements and helpful discussions. **Funding:** The authors acknowledge the supports from the National Science Foundation (DMR-1709116 and ECCS-1912911), the Air Force Office of Scientific Research (AFOSR) (17RT0906), and the FSU Office of Research. TEM work was performed at the National High Magnetic Field Laboratory, which is supported by National Science Foundation Cooperative Agreement No. DMR-1644779, and the State of Florida. **Author contributions:** M.W., Y.T. and B.M. conceived the experiments. M.W. and B.M. analyzed and interpreted the data. M.W.

performed the measurements with help from C.Z., H.L., M.C., L.X., Q.H., D.B., Y.Z. and X.L.; Y.S and Y.X. performed TEM and SAED measurements. The manuscript was written by M.W. and B.M. The project was planned, directed and supervised by B.M. All authors discussed the results and commented on the manuscript. **Competing interests:** The authors declare that they have no competing interests. **Data and materials availability:** All data needed to evaluate the conclusions in the paper are present in the paper and/or the Supplementary Materials. Additional data related to this paper may be requested from the authors.

Figures and Tables

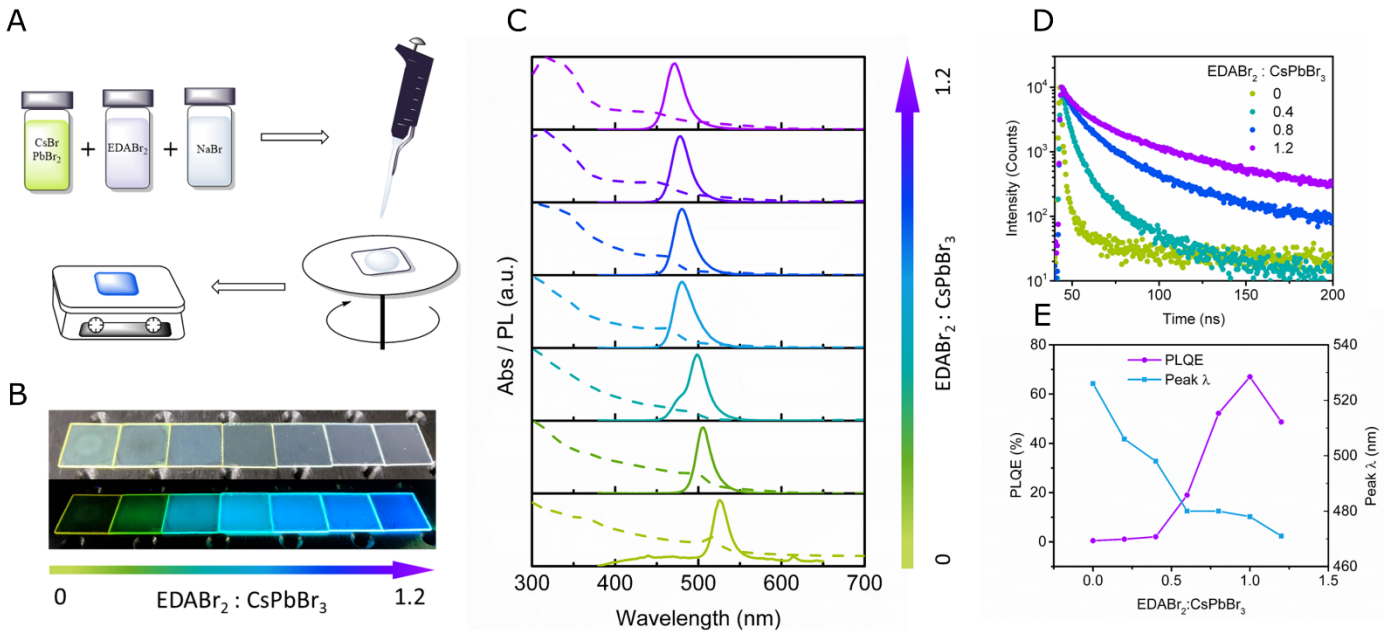

Fig. 1 Processing and photophysical properties of $CsPbBr_3$ thin films containing 3 mol % of NaBr and varying concentrations of $EDABr_2$. (**A**) A schematic showing the one-step spin coating followed by low-temperature thermal annealing. (**B**) Thin films with various concentrations of $EDABr_2$ under ambient light (top) and UV irradiation (bottom). (Photo credit: M.W., Materials Science and Engineering Program, Florida State University) (**C**) Photoluminescence and absorption spectra, (**D**) Time resolved photoluminescence decay curves and (**E**) PLQE and emission peak wavelength of thin films with $EDABr_2$ molar ratio varying from 0 to 1.2 with respect to the perovskite precursors.

Table 1 Composition and photophysical properties of representative thin film samples

Sample	Composition ($CsPbBr_3$: $EDABr_2$: NaBr)	λ_{em}* (nm)	FWHM (nm)	ϕ* (%)	τ_{avg}* (ns)
$CsPbBr_3$	1 : 0 : 0	525	23	0.5	14
$CsPbBr_3$–Na	1 : 0 : 0.03	525	23	0.5	18
EDA5	1 : 1 : 0	498	22	81.5	200
EDA5–Na	1 : 1 : 0.03	478	24	72	150

* λ_{em} is the wavelength at the emission maxima, ϕ is the PLQE; τ_{avg} is the avareage PL lifetime

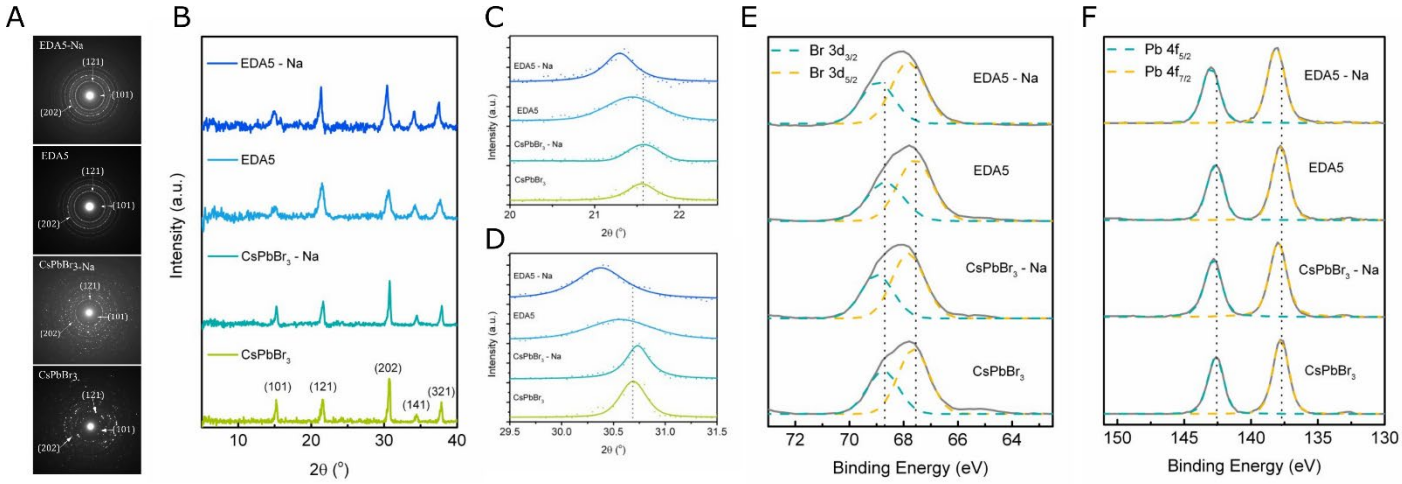

Fig. 2 Structural and surface characterization of thin films. (**A**) Selected area electron diffraction patterns of thin films. (**B**) XRD patterns of thin films. (**C**) Pseudo Voight peak fitting of the diffraction peaks for the (121) and (**D**) (202) crystallographic planes of thin films. Photoelectron spectra from XPS and gaussian peak fitting for (**E**) Br 3d and (**F**) Pb 4f core levels.

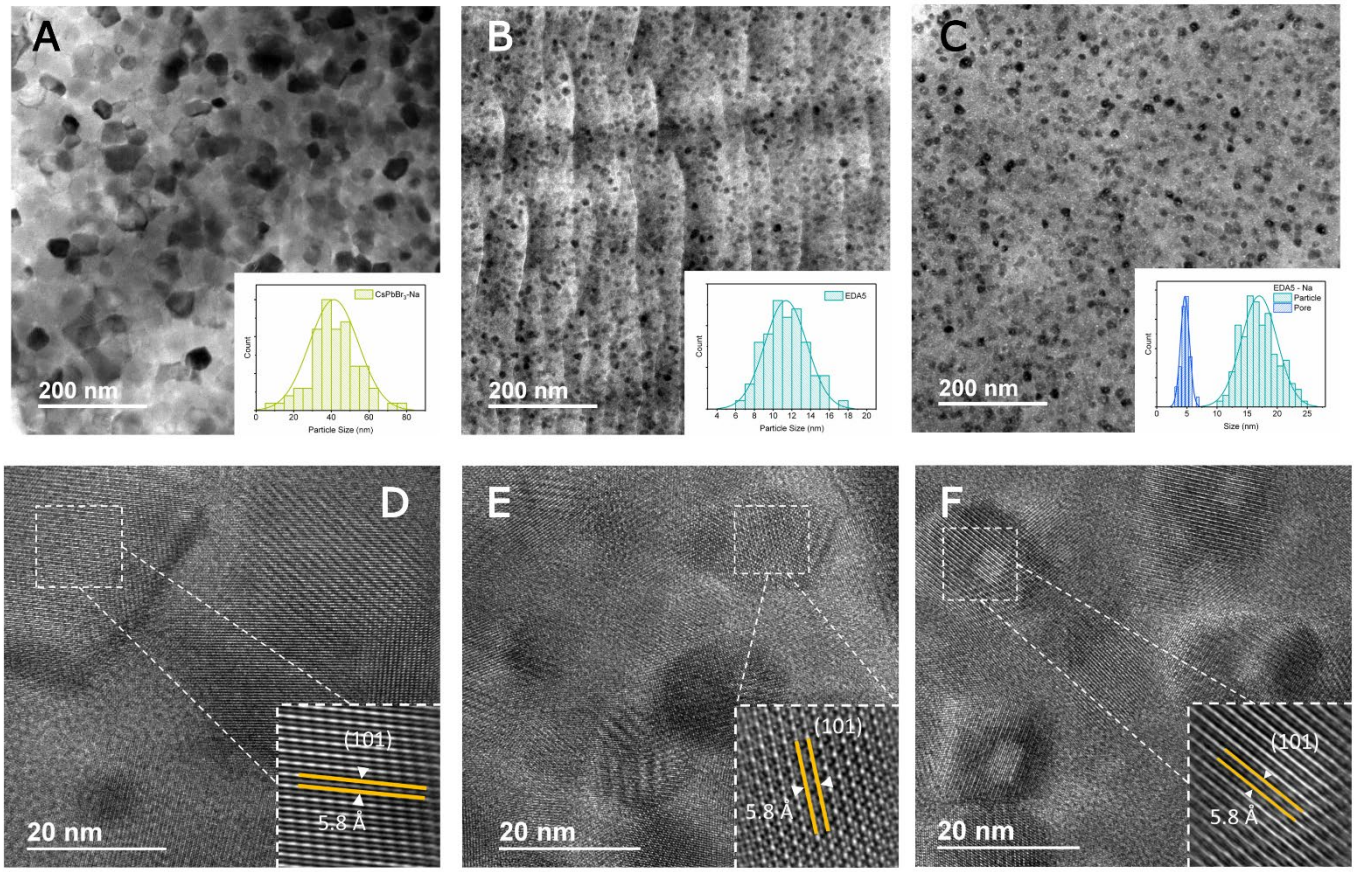

Fig. 3 TEM characterization of thin films. TEM images of (**A**) $CsPbBr_3$-Na, (**B**) EDA5 and (**C**) EDA5-Na thin films. Insets: particle and pore size distribution of NCs. HRTEM images of (**D**) $CsPbBr_3$-Na, (**E**) EDA5, and (**F**) EDA5-Na thin films. Inset: Simulated HRTEM images showing lattice fringes for the (101) planes.

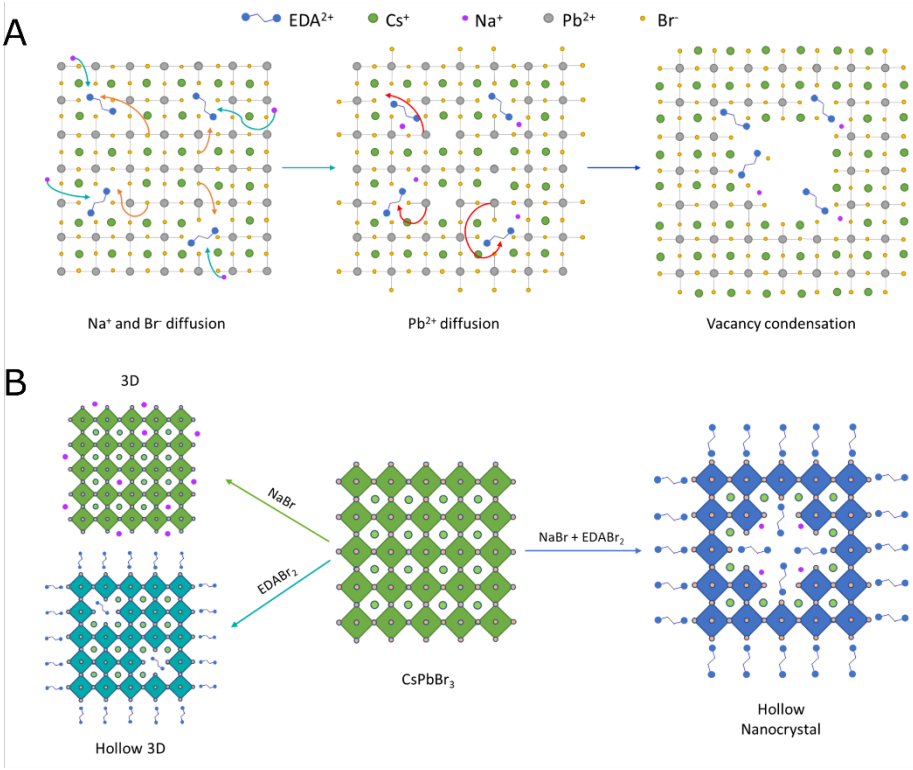

Fig. 4 Proposed formation mechanism and crystal structures. (**A**) proposed formation mechanism of hollow $CsPbBr_3$ NCs beginning from Na^+ and Br^- diffusion from the surface to the core and vice versa, respectively, followed by Pb^{2+} diffusion via Pb^{2+} vacancies culminating in vacancy condensation (**B**) changes of the crystal structures of $CsPbBr_3$ upon the additions of NaBr, $EDABr_2$ and both NaBr and $EDABr_2$.

Science Advances
AAAS

Supplementary Materials

Title

Hollow Metal Halide Perovskite Nanocrystals with Efficient Blue Emissions

Authors

Michael Worku[1], Yu Tian[1†], Chenkun Zhou[2], Haoran Lin[3], Maya Chaaban[3], Liang-jin Xu[3], Qingquan He[3], Drake Beery[3], Yan Zhou[3], Xinsong Lin[3], Yi-feng Su[4], Yan Xin[4] & Biwu Ma*[1, 2, 3]

Affiliations

[1]Materials Science and Engineering Program, Florida State University, Tallahassee, FL 32306, USA.

[2] Chemical and Biomedical Engineering, FAMU-FSU College of Engineering, Florida State University, Tallahassee, FL 32310, USA.

[3]Department of Chemistry and Biochemistry, Florida State University, Tallahassee, FL 32306, USA.

[4]National High Magnetic Field Laboratory, Florida State University, Tallahassee, FL 32310, USA.

[†]Current Address: Global Solar Energy, Tucson, AZ, 85747, USA.

Corresponding author email: bma@fsu.edu

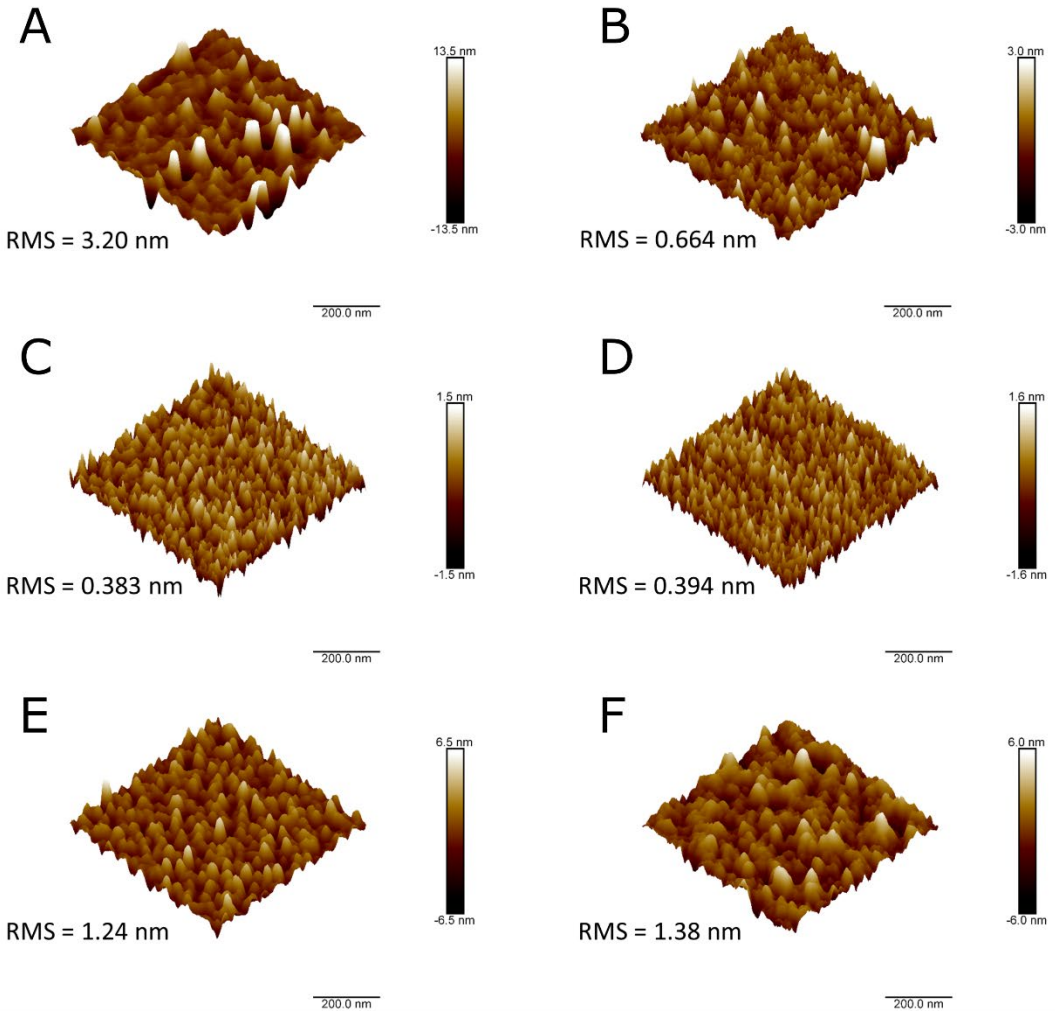

Fig. S1. Atomic Force Microscopy images of thin films. $CsPbBr_3$ thin films containing 3 mol % of NaBr and (**A**) 0.2, (**B**) 0.4, (**C**) 0.6, (**D**) 0.8, (**E**) 1.0 and (**F**) 1.2 molar ratio of $EDABr_2$.

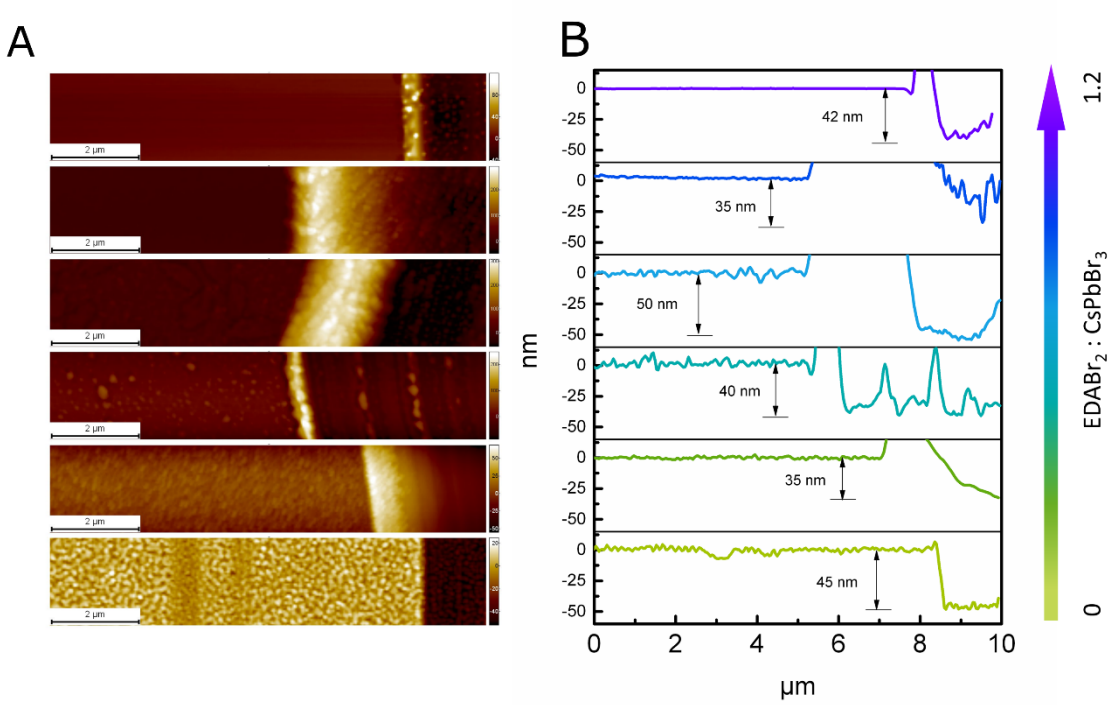

Fig. S2. Thin film thickness. (**A**) An AFM image of a scratched section of a thin film, (**B**) height profile of a transverse section of the corresponding AFM images for $CsPbBr_3$ thin films containing 3 mol % NaBr and varying concentrations of $EDABr_2$.

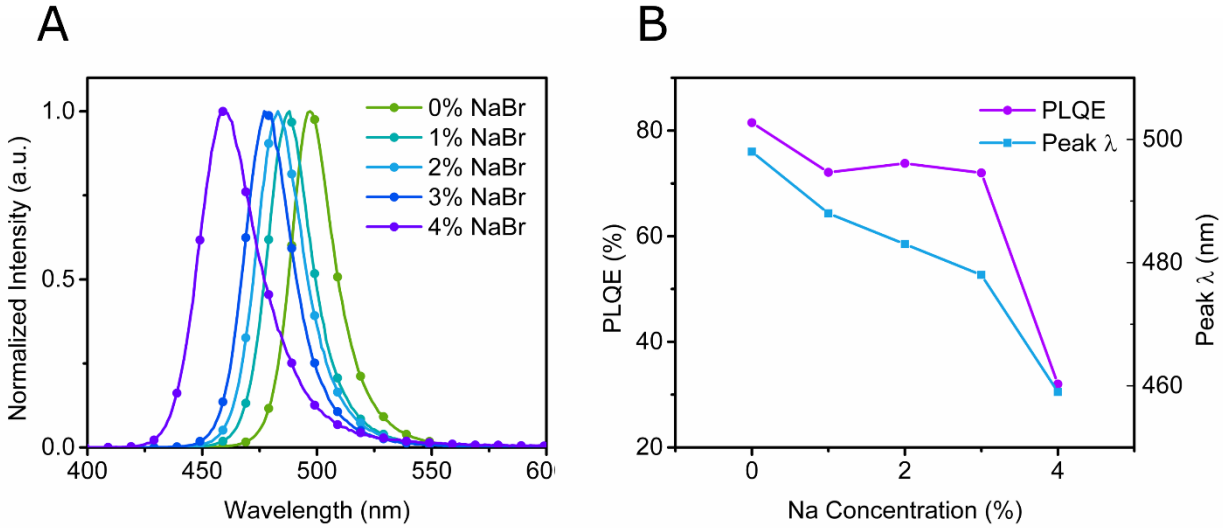

Fig. S3. The effect of NaBr on photophysical properties of $CsPbBr_3$ containing $EDABr_2$. (**A**)Photoluminescence spectra (**B**) PLQE and emission peak wavelength

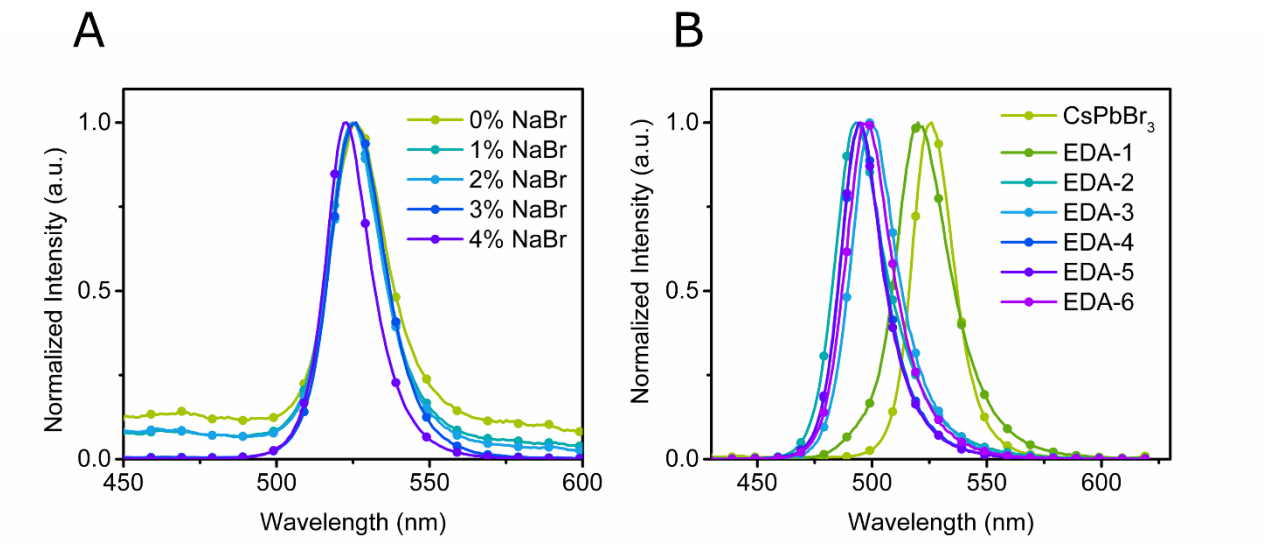

Fig. S4. Photoluminescence spectra of $CsPbBr_3$ thin films with addition of NaBr or $EDABr_2$. (**A**) containing only NaBr and not $EDABr_2$ (**B**) containing $EDABr_2$ and not NaBr.

Table S1 Composition and photophysical properties of samples with varying EDABr2 content

Sample	Composition ($CsPbBr_3$: $EDABr_2$: NaBr)	λ_{em} (nm)	FWHM (nm)	Φ (%)	τ_{avg} (ns)
EDA2-Na	1 : 0.4 : 0.03	498	26	2.1	21
EDA4-Na	1 : 0.8 : 0.03	480	25	52.2	123
EDA6-Na	1 : 1.2 : 0.03	471	25	48.7	146

Table S2. Composition and photophysical properties of samples with varying NaBr content

Sample	Composition ($CsPbBr_3$: $EDABr_2$: NaBr)	λ_{em} (nm)	FWHM (nm)	Φ (%)	τ_{avg} (ns)
1% NaBr	1 : 1 : 0.01	488	22	72.1	119
2% NaBr	1 : 1 : 0.02	483	24	73.8	115
4% NaBr	1 : 1 : 0.04	459	30	32	140

Table S3. Atomic concentrations of samples through XPS

Sample	Composition ($CsPbBr_3$: $EDABr_2$: NaBr)	Br/Pb ratio
$CsPbBr_3$	1 : 0 : 0	2.274
$CsPbBr_3$ – Na	1 : 0 : 0.03	2.329
EDA5	1 : 1 : 0	3.965
EDA5 - Na	1 : 1 : 0.03	4.408

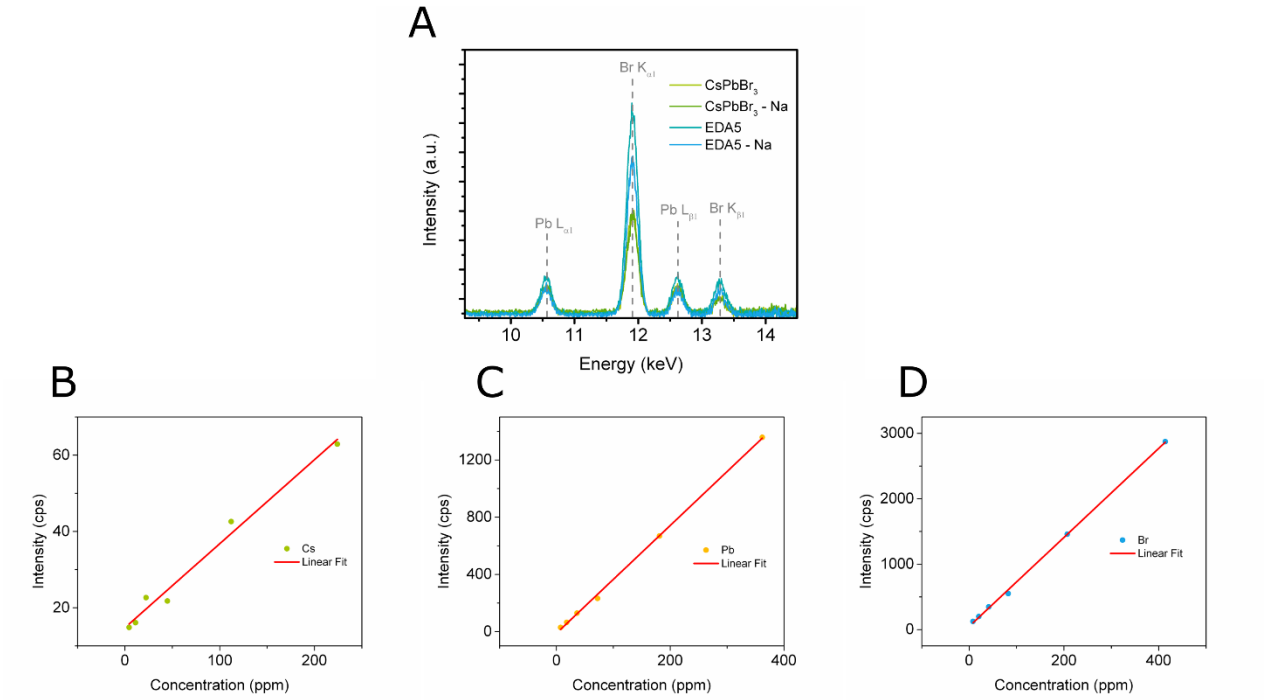

Fig. S5. Energy Dispersive X-ray fluorescence. (**A**) EDXRF spectra. Calibration curves for EDXRF of (**B**) Cs^{+}, (**C**) Pb^{2+}, (**D**) Br^{-}.

78 **Table S4. Quantitative analysis results of EDXRF.**

79

Sample	Ion	Concentration (ppm)	Molarity(M)	Molar ratio
$CsPbBr_3$	Cs^+	19.032	0.1432	0.81
	Pb^{2+}	36.6241	0.17676	1
	Br^-	44.652	0.55882	3.16
$CsPbBr_3$ – Na	Cs^+	31.54	0.23731	1.37
	Pb^{2+}	35.7644	0.17261	1
	Br^-	42.935	0.53733	3.11
EDA5	Cs^+	39.8	0.29946	1.30
	Pb^{2+}	47.56	0.22954	1
	Br^-	96.8828	1.21249	5.28
EDA5 – Na	Cs^+	37.766	0.28416	1.85
	Pb^{2+}	31.855	0.15374	1
	Br^-	69.4152	0.86873	5.65

80

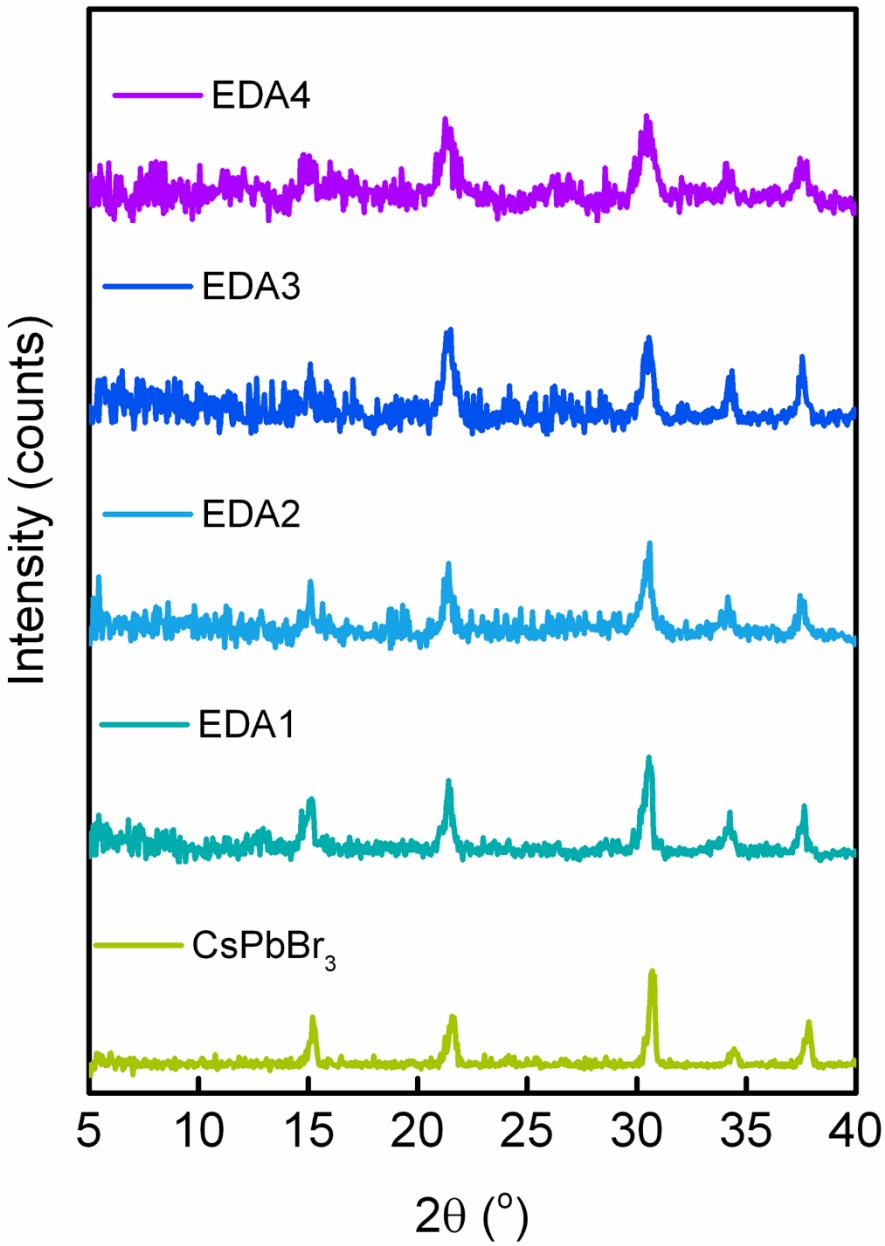

Fig. S6. XRD characterization of thin films with varying $EDABr_2$ content

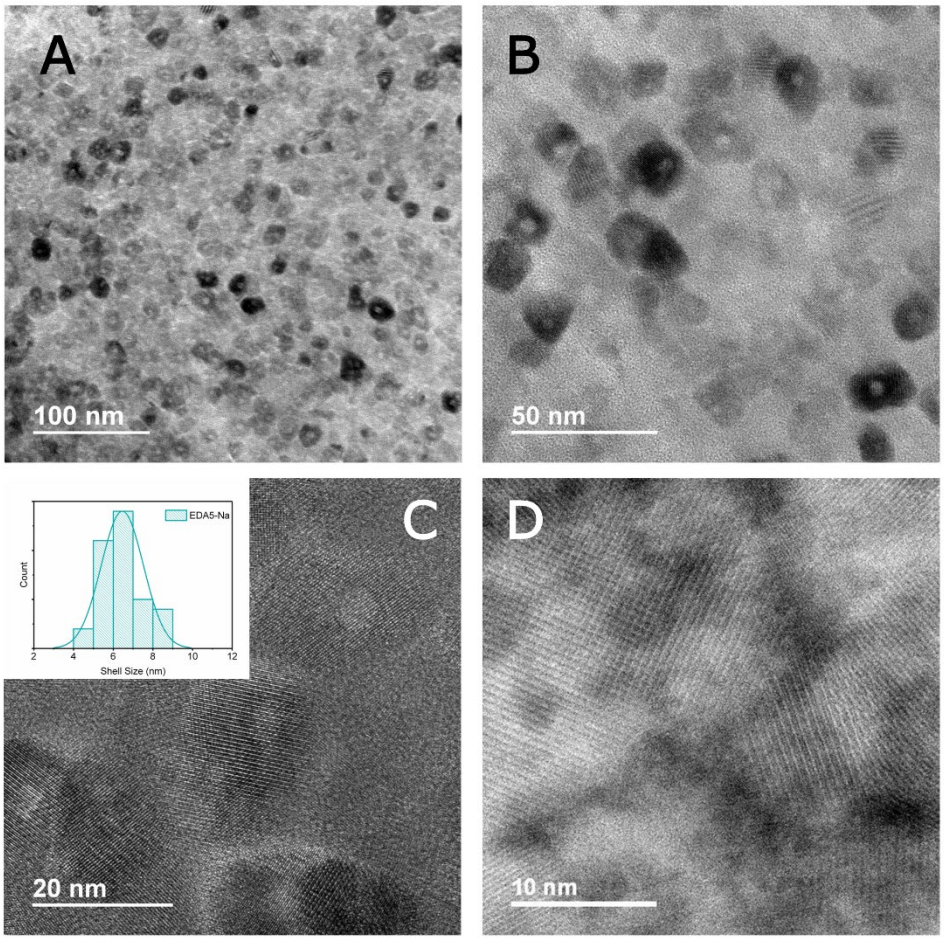

Fig. S7. Microstructural characterization of EDA5-Na. (**A - B**) TEM images of EDA5-Na (**C**) HRTEM image of EDA5-Na (inset: shell thickness size distribution), (**D**) HAADF-STEM image of EDA5-Na.

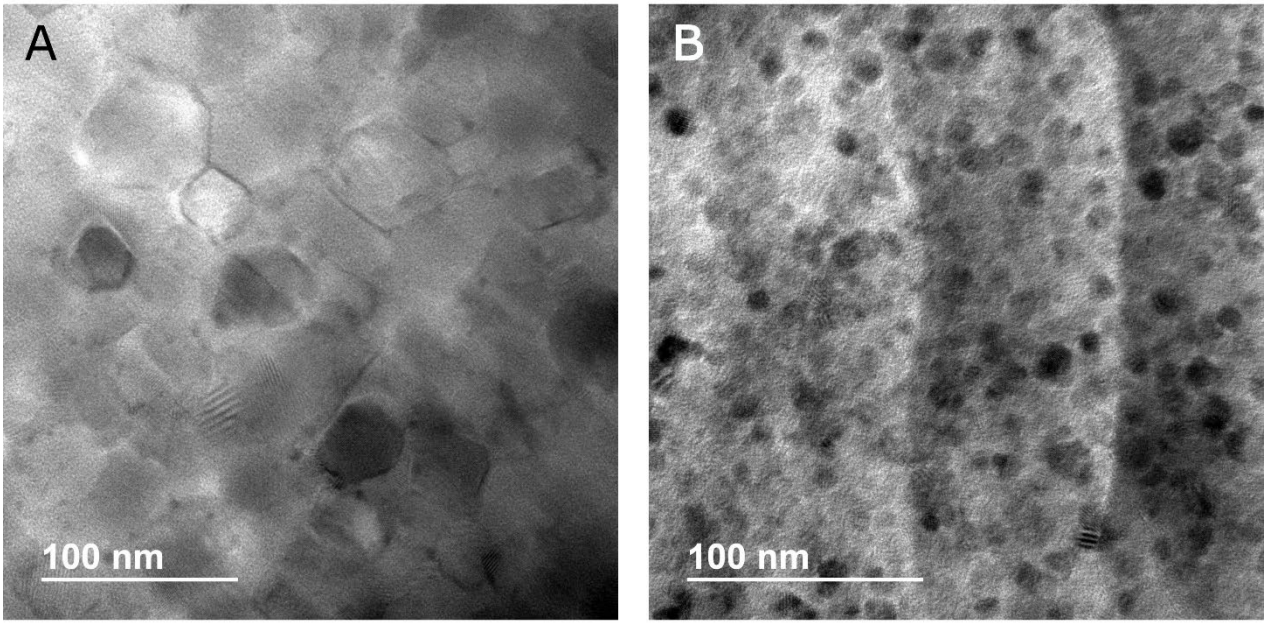

Fig. S8. TEM images of thin films. (**A**) CsPbBr3-Na, (**B**) EDA5.

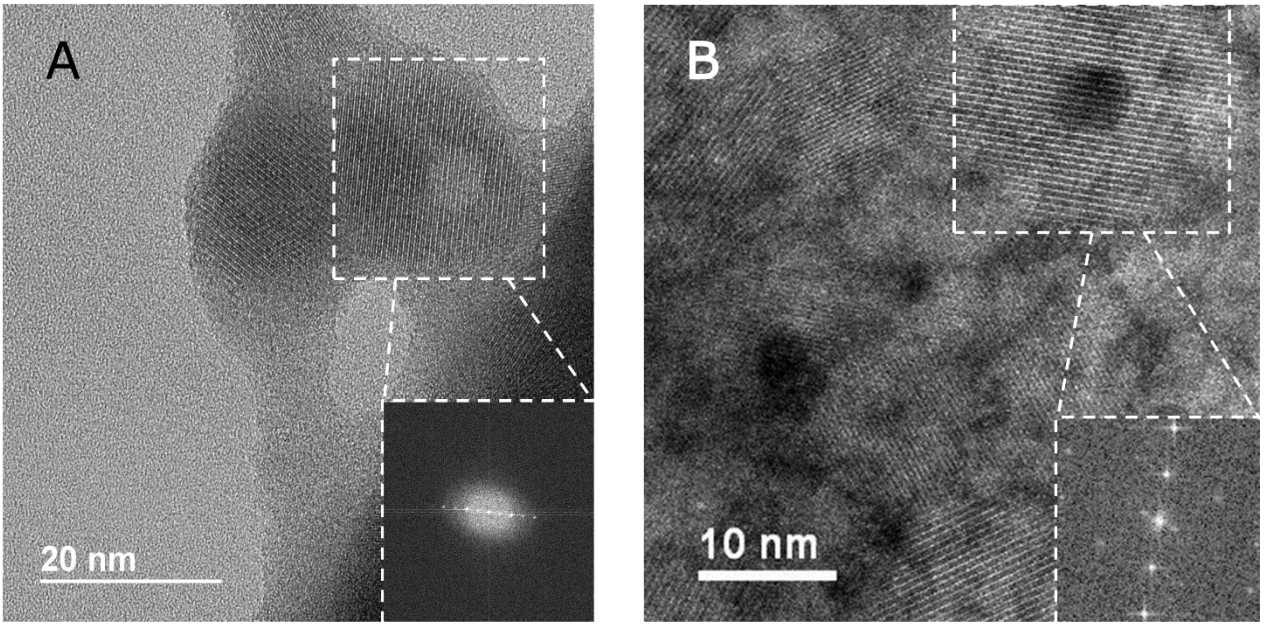

Fig. S9. Mono-grain hollow nanocrystals. (**A**) TEM image of a mono-grain hollow NC (inset: FFT of the marked region), (**B**) STEM image of a mono-grain hollow NC (inset: FFT of marked region).

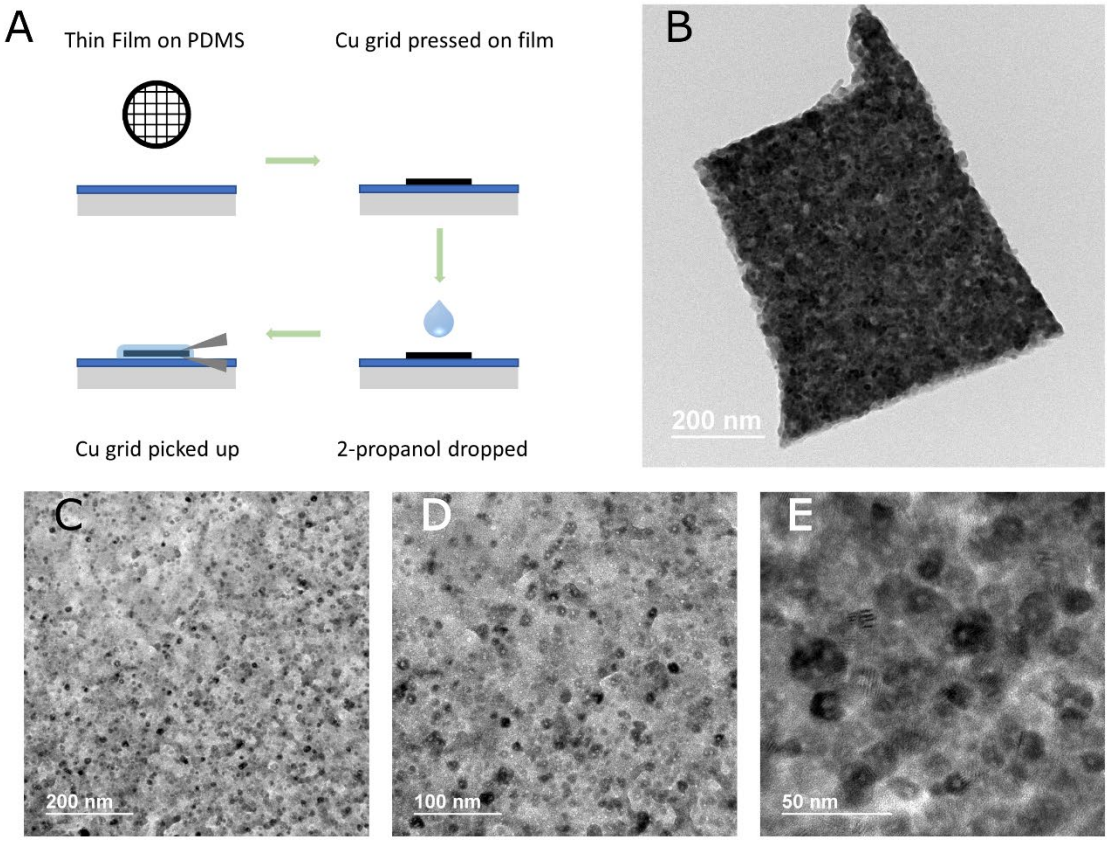

Fig. S10. Alternative TEM sample preparation. (**A**) Cu grid was pressed on thin films formed on PDMS substrate followed by 2-propanol dropping then the Cu grid was picked up with fine tweezers before solvent evaporation, (**B - D**) representative sample under TEM using the described technique.

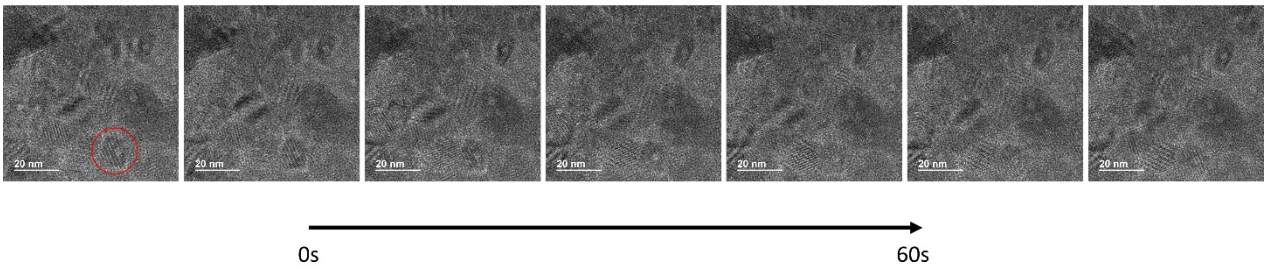

Fig. S11. TEM image as a function of electron beam irradiation time.

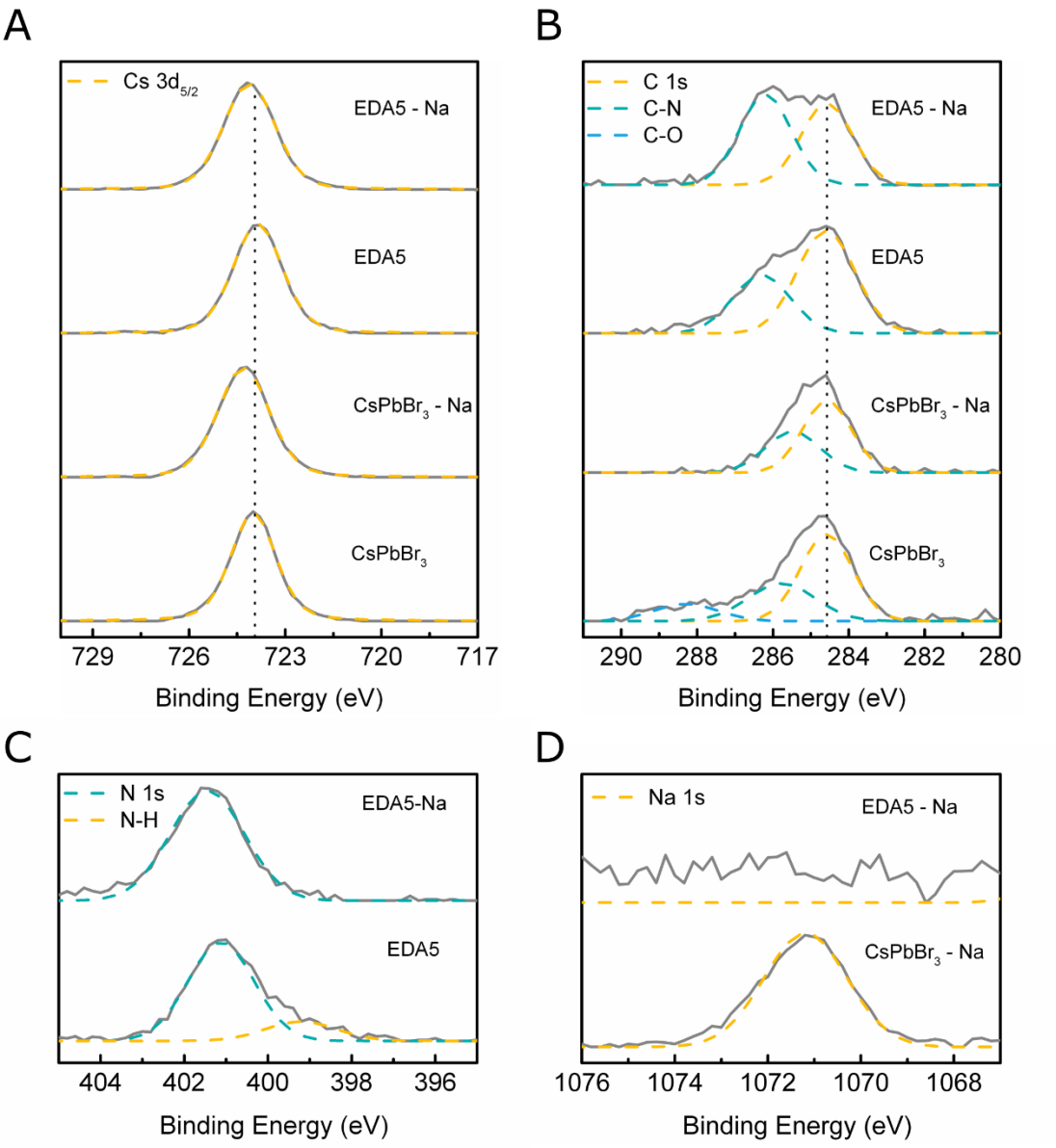

Fig. S12. XPS characterization of thin films. (**A**) Cs 3d peak and Voight fitting of $3d_{5/2}$ and $3d_{3/2}$ peaks (**B**) C 1s peak and gaussian fitting of C-C C 1s and C-N C 1s peaks (**C**) N 1s peak and gaussian fitting of N 1s peak (**D**) Na 1s peak and gaussian fitting Na 1s peak.

We attribute the presence of C-N peaks in $CsPbBr_3$ and $CsPbBr_3$-Na to physiosorbed amine groups during processing.

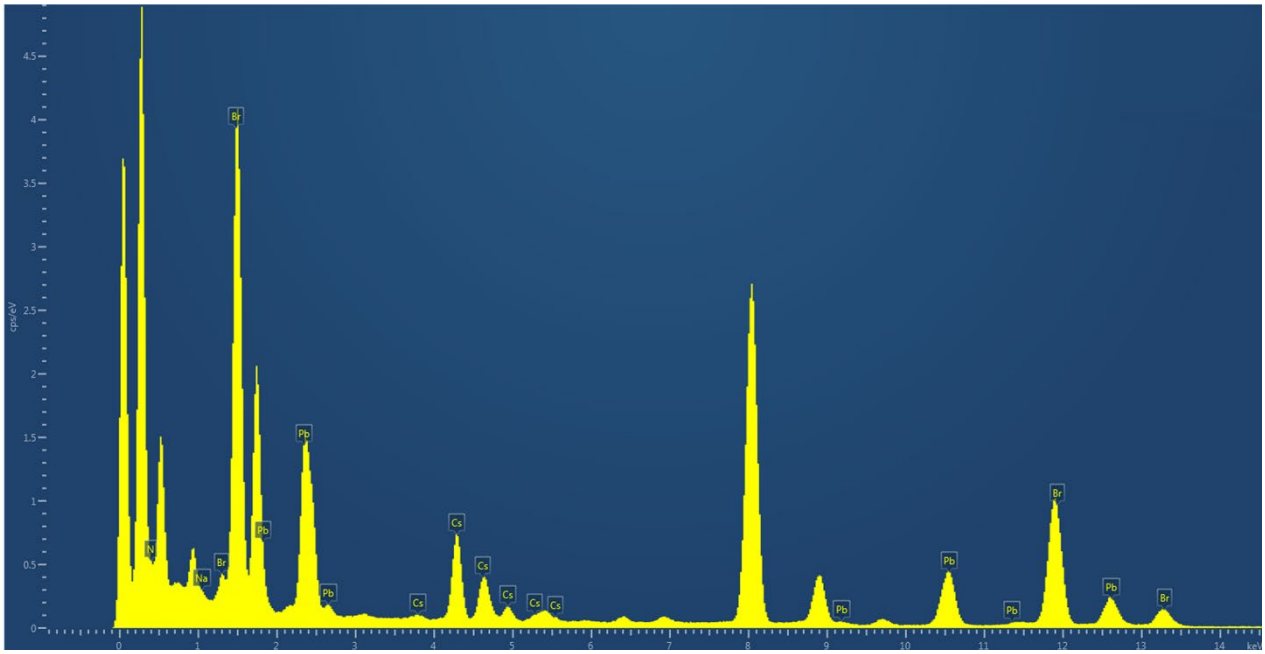

Fig. S13. Energy-dispersive x-ray spectra of EDA5-Na.

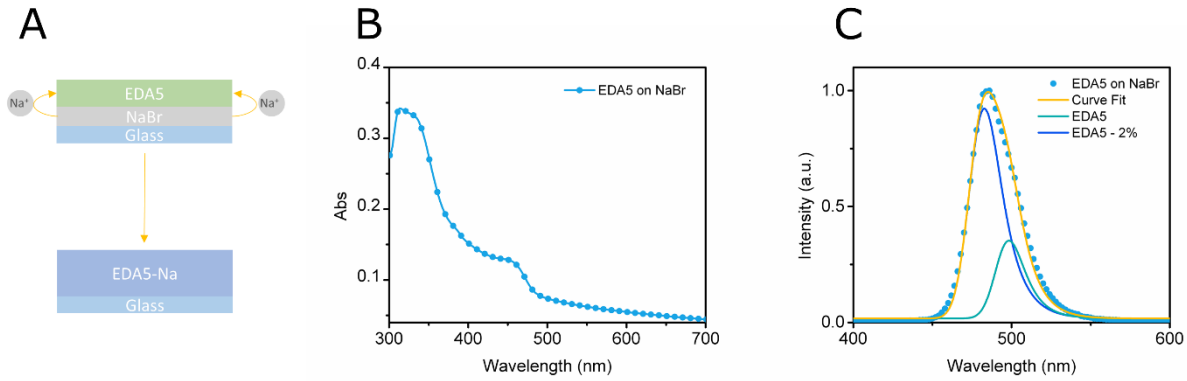

Figure S14. Alternative processing of hollow nanocrystal thin films. (**A**) scheme showing EDA5 thin film cast on 20 nm NaBr layer which under annealing activates Na^+ diffusion from the NaBr layer to the EDA5 layer to form and EDA5-Na thin film, (**B**) UV-Vis absorption spectrum of the processed thin film, (**C**) PL spectrum of as-formed film fit and deconvoluted to the sum of EDA5 and EDA5 with 2 mol % NaBr spectra.

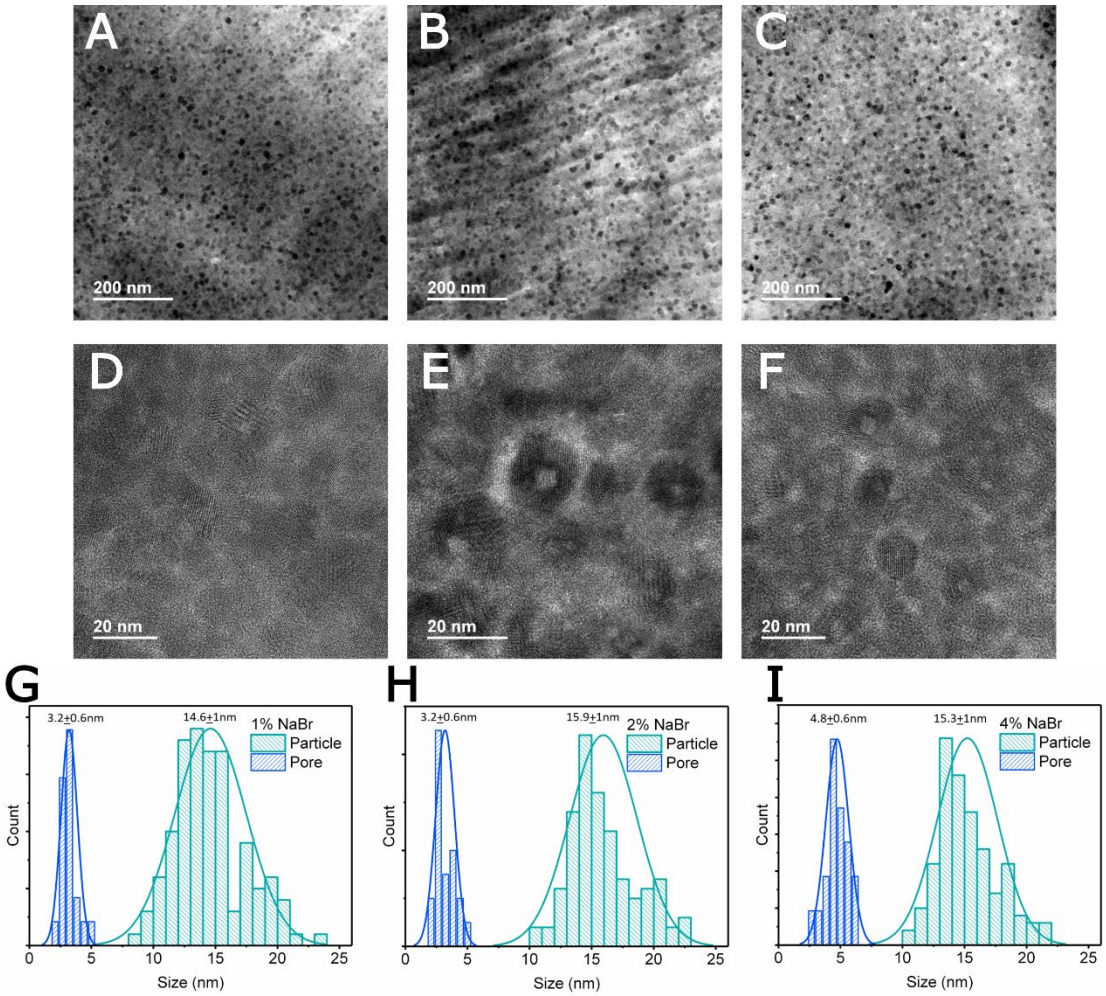

Figure S15. The effect of NaBr content on microstructure. TEM images of $CsPbBr_3$ containing $EDABr_2$ in a 1:1 ratio and (**A**)1 mol% NaBr, (**B**) 2 mol% NaBr, (**C**) 4 mol% of NaBr. HRTEM images of (**D**)1 mol% NaBr, (**E**) 2 mol% NaBr, (**F**) 4 mol% of NaBr. Particle and pore size distributions of (**G**) 1 mol% NaBr, (**H**) 2 mol% NaBr, (**I**) 4 mol% of NaBr.

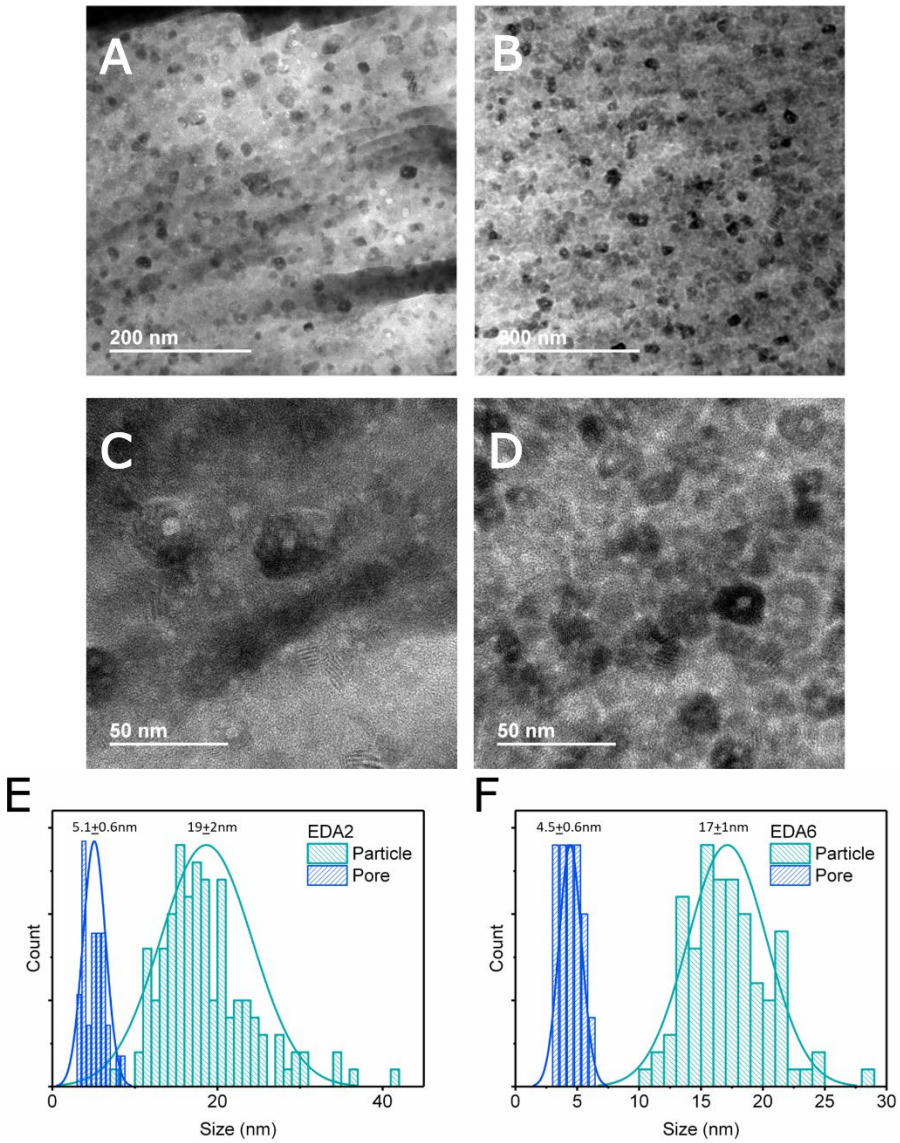

Figure S16. The effect of $EDABr_2$ content on microstructure. TEM images of $CsPbBr_3$ containing 3 mol% of NaBr and $EDABr_2$:$CsPbBr_3$ ratio of (**A**) 0.4, (**B**)1.2. HRTEM images of $EDABr_2$:$CsPbBr_3$ ratio of (**C**) 0.4, (**D**) 1.2. Particle and pore size distributions of $CsPbBr_3$ containing 3 mol% of NaBr and $EDABr_2$:$CsPbBr_3$ ratio of (**E**) 0.4, (**F**) 1.2.